

# Edge states of Floquet-Dirac semimetal in a laser-driven semiconductor quantum-well

Boyuan Zhang,<sup>1</sup> Nobuya Maeshima,<sup>2</sup> and Ken-ichi Hino<sup>3,2,\*</sup>

<sup>1</sup>*Doctoral Program in Materials Science,  
Graduate School of Pure and Applied Sciences,  
University of Tsukuba, Tsukuba, Ibaraki 305-8573, Japan*

<sup>2</sup>*Center for Computational Sciences,  
University of Tsukuba, Tsukuba 305-8577, Japan*

<sup>3</sup>*Division of Materials Science, Faculty of Pure and Applied Sciences,  
University of Tsukuba, Tsukuba 305-8573, Japan*

(Dated: August 17, 2020)

## Abstract

Band crossings observed in a wide range of condensed matter systems are recognized as a key to understand low-energy fermionic excitations that behave as massless Dirac particles. Despite rapid progress in this field, the exploration of non-equilibrium topological states remains scarce and it has potential ability of providing a new platform to create unexpected massless Dirac states. Here we show that in a cw-laser driven semiconductor quantum-well, the optical Stark effect conducts bulk-band crossing, and the resulting Floquet-Dirac semimetallic phase supports an unconventional edge state in the projected one-dimensional Brillouin zone. Further, we reveal that this edge state mediates a transition between topological and non-topological edge states that is caused by tuning the laser intensity. The existence of the respective edge states and the related topological numbers are understood in a unified manner in terms of the laser-induced polarization reflecting parity hybridization in the bulk Brillouin zone.

The theoretical prediction and the subsequent discovery of topological insulators<sup>1,2</sup> have led to explosive expansion of the studies of topological perspectives of condensed matter<sup>3,4</sup> and photonic crystals,<sup>5</sup> where a sharp distinction between topologically trivial and non-trivial phases with energy gaps is made by the presence of a gapless Dirac dispersion. The viewpoint of the gapless state has been developed to connect to the studies of topological semimetals akin to graphene,<sup>6</sup> termed Dirac, Weyl, and line-node semimetals.<sup>7,8</sup> Emergence of topological gapless phases is derived from symmetries inherent in the physical system of concern, namely, the time-reversal (T-)symmetry, the spatial-inversion (I-)symmetry, small groups supported by space groups, and so on.<sup>7-16</sup> As regards a Dirac semimetal (DSM), this is realized by an accidental band crossing due to fine-tuning of material parameters,<sup>9,10</sup> the symmetry-enforced mechanism,<sup>11,12</sup> and the band inversion mechanism.<sup>13-15</sup> Further, there exist edge modes known as double Fermi arcs at the surface of the DSM formed by the band inversion mechanism.<sup>15,17-19</sup> Recently, a growing attention has been paid to two-dimensional (2D) DSMs from the perspective of in-depth theories and applications to novel nano scale devices.<sup>12,16,20-22</sup>

While these intriguing topological semimetals are fabricated in equilibrium, there is still concealed attainability of creating and manipulating gapless Dirac dispersions in Floquet topological systems with spatiotemporal periodicity. Owing to this property, the existence of quasienergy bands are ensured by the Floquet theorem.<sup>23,24</sup> These systems are driven into non-equilibrium states by a temporally periodic external-field that has many degrees of freedom of controlling these states in terms of built-in parameters.<sup>25-31</sup> It is reported that a three-dimensional (3D) DSM, Na<sub>3</sub>Bi, is changed to a Floquet-Weyl semimetal by irradiation of femtosecond laser pulses with a circularly polarized light,<sup>29</sup> and that band crossings at Dirac points are realized by forming a photonic Floquet topological insulator mimicking a graphene-like honeycomb lattice driven by a circularly polarized light.<sup>28</sup> It is remarked that the T-symmetry is broken/protected in a system under the application of a circularly/linearly polarized light-field.

In this study, first, we show that a gapless Dirac state emerges in a 2D-bulk band of a semiconductor quantum well driven by a cw-laser with a linear polarization, where the T-symmetry is protected, however, the I-symmetry is broken. Here, the optical Stark effect (OSE) accompanying quasienergy band splitting<sup>32,33</sup> is introduced to cause an accidental band crossing at high-symmetry points in the 2D Brillouin zone (BZ). This effect is enhanced

by a nearly resonant optical excitation from a valence ( $p$ -orbital) band to a conduction ( $s$ -orbital), as described later in more detail. Such an optically nonlinear excitation leads to strong hybridization between the different parity states with  $s$ - and  $p$ -orbitals over a wide range of the BZ due to the broken I-symmetry. To the best of one's knowledge, there is no study thus far in which the OSE is utilized to generate DSM states. Second, we show that such photoinduced hybridization brings the resulting DSM state to coincide with an unconventional edge state with a linear and nodeful dispersion in a projected one-dimensional (1D) BZ. Further, when the laser intensity changes to make a gap open, this edge state is transformed smoothly into another edge state within this gap; which is either topologically trivial or non-trivial. Finally, we introduce an interband polarization that reflects the degree of parity hybridization in the bulk BZ. Based on this, we show that the zero-value contour of the interband polarization provides the close correspondence between a topological number of Floquet state in the bulk-BZ and the above-mentioned 1D-edge state irrespective of being topologically trivial or non-trivial.

These edge states concerned here share features with other studies. As regards the OSE, a valley-selective OSE is demonstrated in monolayer transition metal dichalcogenides with application of a circularly polarized electric field.<sup>34</sup> As regards edge states of the Floquet DSM states, Tamm states<sup>35–37</sup> appearing in the surfaces of several Dirac materials are theoretically examined.<sup>38</sup> Recently, growing interest has been captured in the interrelation of Tamm states with topological edge states in optical waveguide arrays,<sup>39–42</sup> 1D photonic crystals,<sup>43–45</sup> a graphene ring with the Aharonov-Bohm effect,<sup>46</sup> a honeycomb magnon insulator,<sup>47</sup> and a gold surface.<sup>48</sup>

## Results

**Modified Bernevig-Hughes-Zhang model with a laser-electron interaction.** We begin by constructing the Hamiltonian of the present system of a semiconductor quantum well with a linearly polarized light field based on the paradigmatic Bernevig-Hughes-Zhang (BHZ) model<sup>2</sup> composed of two bands with  $s$ - and  $p$ -orbitals in view of a spin degree of freedom. Hereafter, the band with  $s(p)$ -orbital is termed as  $s(p)$ -band just for the sake of simplicity, and the atomic units (a.u.) are used throughout unless otherwise stated. The

BHZ Hamiltonian concerned here is read as the  $4 \times 4$ -matrix:

$$\mathcal{H}_{\text{BHZ}}(\mathbf{k}) = \epsilon(\mathbf{k})I + \sum_{i=3}^5 d_i(\mathbf{k})\Gamma_i \quad (1)$$

with  $\mathbf{k} = (k_x, k_y)$  as a 2D Bloch momentum defined in the  $xy$ -plane normal to the direction of crystal growth of quantum well, namely, the  $z$ -axis. Here  $I$  represents the  $4 \times 4$  unit matrix, and  $\Gamma_j$ 's represent the four-dimensional Dirac matrices for the Clifford algebra, defined by  $\Gamma_1 = \tau_x \otimes \sigma_x$ ,  $\Gamma_2 = \tau_x \otimes \sigma_y$ ,  $\Gamma_3 = \tau_x \otimes \sigma_z$ ,  $\Gamma_4 = \tau_z \otimes I_2$ , and  $\Gamma_5 = \tau_y \otimes I_2$ , where  $I_2$  represents the  $2 \times 2$  unit matrix,  $\tau_s$  and  $\sigma_s$  with  $s = x, y, z$  represent the Pauli matrices for orbital and spin degrees of freedom, respectively, and the anti-commutation relation,  $\{\Gamma_i, \Gamma_j\} = 2\delta_{ij}$ , is ensured. Further,  $\epsilon(\mathbf{k}) = \frac{1}{2}(\epsilon_s + \epsilon_p) - (t_{ss} - t_{pp})(\cos k_x a + \cos k_y a)$ , and

$$\begin{cases} d_3(\mathbf{k}) = 2t_{sp} \sin k_y a \\ d_4(\mathbf{k}) = \frac{1}{2}(\epsilon_s - \epsilon_p) - (t_{ss} + t_{pp})(\cos k_x a + \cos k_y a) , \\ d_5(\mathbf{k}) = 2t_{sp} \sin k_x a \end{cases} \quad (2)$$

where  $\epsilon_b$  and  $8t_{bb}$  represent the center and width of band  $b$ , respectively, and  $t_{bb'}$  represents a hopping matrix between  $b$  and  $b'(\neq b)$  orbitals with lattice constant  $a$ ; after this,  $a$  is set equal to unity. Hereafter, a semiconductor quantum well of HgTe/CdTe is accounted as the object of material. It is understood that  $t_{ss} = t_{pp}$  and  $\epsilon_s = -\epsilon_p$ . Thus, a Fermi energy is given by  $E_F = (\epsilon_s + \epsilon_p)/2 = 0$ , and the energy gap  $E_g$  at the  $\Gamma$ -point of the quantum well equals  $2(\epsilon_s - 4t_{ss})$ .

An interaction of electron with a laser field is introduced into  $\mathcal{H}_{\text{BHZ}}(\mathbf{k})$  by replacing  $\mathbf{k}$  by  $\mathbf{K}(t) = \mathbf{k} + \mathbf{A}(t)$ , followed by adding to  $\mathcal{H}_{\text{BHZ}}(\mathbf{K}(t))$  an interband dipole interaction given by  $v(t) = \Omega(t)\Gamma_6$ , where  $\Gamma_6 = \tau_x \otimes I_2$ , and  $\Omega(t)$  is a real function of time  $t$ , provided as  $\Omega(t) = \mathbf{F}(t) \cdot \mathbf{X}_{sp}$ . Here an electric field of the cw-laser with a linear polarization in the  $x$ -direction is given by  $\mathbf{F}(t) = (F_x \cos \omega t, 0, 0)$  with a constant amplitude  $F_x$  and a frequency  $\omega$ , where this is related with a vector potential  $\mathbf{A}(t)$  as  $\mathbf{F}(t) = -\dot{\mathbf{A}}(t)$ , and  $\mathbf{X}_{sp} = (X_{sp}, 0, 0)$  represents a matrix element of electric dipole transition between  $s$ - and  $p$ -orbitals, independent of  $\mathbf{k}$ :  $\mathbf{X}_{sp} = \mathbf{X}_{ps}^*$ . Thus, in place of  $\mathcal{H}_{\text{BHZ}}(\mathbf{k})$ , the resulting expression ends with up

$$H(\mathbf{k}, t) = \mathcal{H}_{\text{BHZ}}(\mathbf{K}(t)) + v(t) \equiv \sum_{i=3}^6 D_i(\mathbf{k}, t)\Gamma_i, \quad (3)$$

where  $D_i(\mathbf{k}, t) = d_i(\mathbf{K}(t))$  for  $i \neq 6$ , and  $D_6(\mathbf{k}, t) = \Omega(t)$ . Obviously, this ensures the

temporal periodicity,  $H(\mathbf{k}, t + T) = H(\mathbf{k}, t)$ , with  $T = 2\pi/\omega$ , and the system of concern follows the Floquet theorem.

**T- and pseudo-I-symmetries.** It is evident that the T- and I-symmetries are conserved in  $\mathcal{H}_{\text{BHZ}}(\mathbf{k})$ , that is,  $\Theta^{-1} \mathcal{H}_{\text{BHZ}}(-\mathbf{k})\Theta = \mathcal{H}_{\text{BHZ}}(\mathbf{k})$ , and  $\Pi^{-1} \mathcal{H}_{\text{BHZ}}(-\mathbf{k})\Pi = \mathcal{H}_{\text{BHZ}}(\mathbf{k})$ , where  $\Theta$  and  $\Pi$  represent the T- and I-operators, defined by  $\Theta = -iI_2 \otimes \sigma_y K$  and  $\Pi = \tau_z \otimes I_2$ , respectively, where  $K$  means an operation of taking complex conjugate. Accordingly, by fine-tuning  $E_g$ , it is likely that an accidental band crossing occurs at a high-symmetry point with four-fold degeneracy.<sup>9</sup>

On the other hand, as regards  $H(\mathbf{k}, t)$ , while the T-symmetry is still respected, the I-symmetry is broken because  $D_i(-\mathbf{k}, t) \neq -D_i(\mathbf{k}, t)$  for  $i = 3, 5, 6$ , and  $D_4(-\mathbf{k}, t) \neq D_4(\mathbf{k}, t)$ . That is,  $\Theta^{-1}H(-\mathbf{k}, -t)\Theta = H(\mathbf{k}, t)$ , whereas  $\Pi^{-1}H(-\mathbf{k}, t)\Pi \neq H(\mathbf{k}, t)$ . In fact, it is shown that in terms of an operator defined as  $\tilde{\Pi} = \Pi\mathcal{T}_{1/2}$ , the symmetry  $\tilde{\Pi}^{-1}H(-\mathbf{k}, t + T/2)\tilde{\Pi} = H(\mathbf{k}, t)$  is retrieved, where  $\mathcal{T}_{1/2}$  represents the operation of putting  $t$  ahead by a half period  $T/2$ , namely, the replacement of  $t \rightarrow t + T/2$ , and hereafter  $\tilde{\Pi}$  is termed as the pseudo-I operator.

**Floquet quasienergy bands.** Owing to the Floquet theorem, a wavefunction of the time-dependent Schrödinger equation for  $H(\mathbf{k}, t)$  is expressed as  $\Psi_{\mathbf{k}\alpha}(t)e^{-iE_\alpha(\mathbf{k})t}$  for Floquet state  $\alpha$ , and thus  $\Psi_{\mathbf{k}\alpha}(t)$  is ensured by the quasi-stationary equation

$$L(\mathbf{k}, t)\Psi_{\mathbf{k}\alpha}(t) = E_\alpha(\mathbf{k})\Psi_{\mathbf{k}\alpha}(t) \quad (4)$$

under a temporally periodic condition  $\Psi_{\mathbf{k}\alpha}(t+T) = \Psi_{\mathbf{k}\alpha}(t)$ , where  $L(\mathbf{k}, t) = H(\mathbf{k}, t) - iI\partial/\partial t$  and  $E_\alpha(\mathbf{k})$  is an eigenvalue termed as quasienergy of the 2D bulk band. It is noted that  $\Theta^{-1}L(-\mathbf{k}, -t)\Theta = L(\mathbf{k}, t)$ , and  $\tilde{\Pi}^{-1}L(-\mathbf{k}, t + T/2)\tilde{\Pi} = L(\mathbf{k}, t)$ . The state  $\alpha$  is denoted as a combination of  $\beta(n)$ , where  $\beta$  is assigned to either  $s$ - or  $p$ -band that dominates over this hybridized state, and  $n$  represents an additional quantum number due to the temporal periodicity that means the number of dressing photons. It is remarked that there is a relation,  $E_{\beta(n+N)}(\mathbf{k}) = E_{\beta(n)}(\mathbf{k}) + N\omega$ , with  $N$  an integer. Owing to the pseudo-I-symmetry,  $E_\alpha(\mathbf{k})$  equals  $E_\alpha(-\mathbf{k})$ , where the associated eigenstate of the former is  $\Psi_{\mathbf{k}\alpha}(t)$ , while that of the latter is  $\tilde{\Pi}\Psi_{\mathbf{k}\alpha}(t) = \Psi_{-\mathbf{k}\alpha}(t + T/2)$ . Thus, a component  $(\alpha', \alpha)$  of a representation matrix of  $\tilde{\Pi}$  is given by  $\frac{1}{T} \int_0^T dt \langle \Psi_{-\mathbf{k}\alpha'}(t) | \Psi_{-\mathbf{k}\alpha}(t + T/2) \rangle$ . It is remarked that a parity is still a good quantum number at a high-symmetry point  $\mathbf{k} = \mathbf{k}^j$  ( $j = \Gamma, X_1, X_2, M$ ), that is,

$\Pi^{-1}L(\mathbf{k}^j, t)\Pi = L(\mathbf{k}^j, t)$ , where four  $X$ -points in the 2D-BZ are not equivalent, because the application of the laser field in the  $x$ -direction breaks the  $C_4$  symmetry around the  $z$ -axis, and thus, these are distinguished by representing as  $X_1$  and  $X_2$ .

$E_\alpha(\mathbf{k})$ 's are obtained by numerically solving Eq. (4) in the frequency ( $\omega$ ) domain, where the Floquet matrix is recast into  $\tilde{L}_{nn'}(\mathbf{k}, \omega) = (n|L(\mathbf{k}, t)|n')$  with respect to  $n$  and  $n'$  photon states; it is understood that  $(n|\cdots|n') = \frac{1}{T} \int_0^T dt e^{-i(n-n')\omega t} \cdots$ . The matrix element of it is read as

$$\tilde{L}_{nn'}(\mathbf{k}, \omega) = n\omega\delta_{nn'}I + \sum_{i=3}^6 \tilde{D}_{i,nn'}(\mathbf{k}, \omega)\Gamma_i, \quad (5)$$

where  $\tilde{D}_{i,nn'}(\mathbf{k}, \omega) = (n|D_i(\mathbf{k}, t)|n')$ , and an explicit expression of it is given in Supplementary Note 1. On the other hand, as regards a quasienergy band,  $\mathcal{E}_\alpha(k_x)$ , which is the projection of  $E_\alpha(\mathbf{k})$  onto the  $k_x$ -direction, one applies to Eq. (4) in view of Eq. (5) the lattice representation in the  $y$ -direction where the motion of electron is confined, followed by solving it under vanishing boundary conditions imposed on two edges.

**Quasienergy-band inversion and crossing due to OSE.** Here we show an overall change of quasienergy spectra with respect to  $F_x$  due to the OSE, eventually leading to a band inversion. Figure 1 shows the scheme of the nearly resonant optical-excitation from the  $p$ -band to  $s$ -band with  $\omega \lesssim E_g$ . Such a scheme of excitation almost maximizes the degree of the  $sp$  hybridization to induce sharp quasienergy-splitting of the order of  $\Omega_R$  between two quasienergy bands of  $s(n-1)$  and  $p(n)$  for  $n = 0, 1$ , where  $\Omega_R$  represents the Rabi frequency given by  $F_x X_{sp}$ .<sup>32</sup> As  $F_x$  increases, a pair of photodressed bands of  $p(1)$  and  $s(-1)$  undergoes inversion to swerve with anticrossing.

Figures 2a and 2b show the calculated results of  $\mathcal{E}_{p(1)}(k_x)$  and  $\mathcal{E}_{s(-1)}(k_x)$  as a function of  $F_x$  for  $k_x = 0$  and  $\pi$ , respectively. It is noted that these bands cross at the abscissa ( $\mathcal{E}(k_x) = E_F = 0$ ) without anticrossings at  $F_x$ 's indicated by I, II, and III; these positions are mentioned as  $F_x^{\text{I}}$ ,  $F_x^{\text{II}}$ , and  $F_x^{\text{III}}$ , respectively. The band inversions of  $p(1)$  and  $s(-1)$  discerned in Figs. 2a and 2b accompany the emergence of zero-energy modes indicative of topological phase transitions, where the zero-energy modes are designated by the horizontal lines along the abscissa in  $F_x^{\text{II}} < F_x < F_x^{\text{I}}$  and  $F_x < F_x^{\text{III}}$ , respectively.

To examine the band crossings in detail, bulk bands  $E(\mathbf{k})$  at  $F_x^{\text{I}}$ ,  $F_x^{\text{II}}$ , and  $F_x^{\text{III}}$  are shown in Figs. 3a-3c, where  $E_{p(1)}(\mathbf{k})$  and  $E_{s(-1)}(\mathbf{k})$  are degenerate at a single point of  $\mathbf{k}^j$  in the 2D-BZ with  $j = \Gamma$ ,  $X_2$ , and  $X_1$ , respectively; these are indicated in Fig. 3d. Obviously, the

crossing points seen in Fig. 2 are found identical with these high-symmetry points projected on the  $k_x$ -axis, which are denoted as  $\bar{\Gamma} = \bar{X}_2$  and  $\bar{X}_1 = \bar{M}$ . Actually,  $E(\mathbf{k})$  is conical-shaped with linear-dispersion in the vicinity of  $\mathbf{k}^j$ , and this is considered as a DSM state. It is understood that hereafter,  $F_x^I, F_x^{II}$ , and  $F_x^{III}$  are represented as  $F_x^\Gamma, F_x^{X_2}$ , and  $F_x^{X_1}$ , respectively.

**Fourfold accidental degeneracy and a  $\sigma_z$ -non-conserving interaction.** Here we consider the origin of such band crossings. Because of the conservation of both T- and pseudo-I-symmetries, it is still probable that the band crossing between  $p(n)$  and  $s(n')$  occurs at a high-symmetry point. In fact, to that end, an additional condition is required that the difference of photon numbers  $\Delta n \equiv n - n'$  is an even number, as is proved rigorously in Supplementary Note 2. As long as just a single  $4 \times 4$ -block matrix comprised of two components,  $p(n_0)$  and  $s(n'_0 \equiv n_0 - \Delta n)$ , for a specific  $n_0$  is concerned in Eq. (5), this condition is intuitively convinced by seeing that  $\tilde{D}_{i,n_0n'_0}(\mathbf{k}^j, \omega) = 0$  with  $i = 3, 5, 6$  when  $\Delta n$  is even — because of odd functions with respect to  $\mathbf{k}$  —, as shown in Supplementary Note 1, and that the remaining term  $\tilde{D}_{4,n_0n'_0}(\mathbf{k}^j, \omega)$  is made vanish by fine-tuning  $F_x$ . Contrariwise, when  $\Delta n$  is odd, the resulting pair of bands are gapped out; especially, the two bands  $p(1)$  and  $s(0)$  never cross. The above-mentioned condition holds exact in general even for  $E_{p(1)}(\mathbf{k})$  and  $E_{s(-1)}(\mathbf{k})$  that are obtained beyond this simplest two-component model.

Next, we consider the effect of a  $\sigma_z$ -non-conserving interaction on the obtained results, which is given by

$$v_z(\mathbf{k}, t) = \sum_{i=1,2} D_i(\mathbf{k}, t) \Gamma_i, \quad (6)$$

where  $D_i(\mathbf{k}, t) = d_i(\mathbf{K}(t))$ , and  $d_i(\mathbf{k})$ 's are odd functions with respect to  $\mathbf{k}$  to keep  $v_z(\mathbf{k}, t)$  both T- and pseudo-I-symmetric. Based on the two-component model, when  $\Delta n$  is even, it is evident that a gap remains closed because of  $\tilde{D}_{i,n_0n'_0}(\mathbf{k}^j, \omega) = 0$  with  $i = 1, 2$ . Similarly to the above case of the  $\sigma_z$ -conserving interactions, this still hold in general, as is verified in Supplementary Note 2.

**DSM state and edge state.** Here we examine the 1D-band  $\mathcal{E}(k_x)$  and a concomitant edge state that is either topologically trivial or non-trivial; hereafter, it is understood that the term of the Tamm state<sup>38</sup> is used exclusively to mean a trivial state bound on an edge to distinguish it from a non-trivial one. Figures 4a-4c, 5a-5c, and 6a-6c show the spectra of

$\mathcal{E}(k_x)$  in the decreasing order of  $F_x$ . It is seen that all the DSM states delimits the boundary of a topological phase transition (see Figs. 4b, 5b, and 6b). It should be noted that the DSM states observed at  $F_x^{X_2}$  and  $F_x^{X_1}$  coincide with edge states with linear and nodeful dispersions (see Fig. 5b, and Fig 6b, respectively), differing from that observed at  $F_x^\Gamma$  (see Fig. 4b). Such edge states are termed the Dirac-Tamm state hereafter just for the sake of convenience of making a distinction from other Tamm states. As regards the Dirac-Tamm state at  $F_x^{X_2}$ , with the slight increase of  $F_x$  to make a gap open, this is transformed into an unequivocally topological edge state with its band structure kept almost as it stands (see Fig. 5a), while with the change of  $F_x$  in the opposite direction, this becomes nodeless with two flat dispersions (see Fig. 5c). As regards the Dirac-Tamm state at  $F_x^{X_1}$ , with the slight increase of  $F_x$ , this is transformed into a nodeless edge state (see Fig. 6a), while with the slight decrease of  $F_x$ , this becomes unequivocally topologically trivial (see Fig. 6c).

The topological nature of these edge states is evaluated, relying on the bulk-boundary correspondence, in terms of the Chern number of state  $\alpha$  given by

$$C_\alpha = \frac{1}{2\pi} \oint d\mathbf{k} \cdot \mathbf{a}_\alpha(\mathbf{k}), \quad (7)$$

where the Berry connection is defined by  $\mathbf{a}_\alpha(\mathbf{k}) = -\frac{i}{T} \int_0^T dt \langle \Psi_{\mathbf{k}\alpha}(t) | \nabla_{\mathbf{k}} \Psi_{\mathbf{k}\alpha}(t) \rangle$ . Here,  $\alpha$  is set the lower band, denoted as  $\alpha_L$ , where  $E_{\alpha_L}(\mathbf{k}) \leq E_F = 0$ . It is confirmed that the non-zero values of  $C_{\alpha_L} = 1$  are obtained in  $F_x^{X_2} < F_x < F_x^\Gamma$  and  $F_x < F_x^{X_1}$ , otherwise this vanishes. Thus, we verify that the edge state observed in  $F_x^{X_1} < F_x < F_x^{X_2}$  is a Tamm state. Further, the Dirac-Tamm states at  $F_x^{X_1}$  and  $F_x^{X_2}$  are also considered Tamm states, since their respective net Chern numbers are zero.<sup>8</sup> To the best of one's knowledge regarding edge/surface states of DMS, there exists a theoretical study showing that a nodal surface state — akin to a Dirac-Tamm state — is supported by a 3D massless Dirac fermion, based on a two-band model of the Dirac equation.<sup>38</sup> Further, it is reported that double Fermi arcs are formed at the surface of a 3D-DSM phase that is created by the band inversion mechanism.<sup>8,15,17–19</sup>

**Interband polarization.** To deepen the understanding of the two types of edge states, namely, the topological edge state and the Tamm state, a macroscopic polarization of the present system, that is, an induced dipole moment, is examined. This is given by

$$D_{\mathbf{k}\alpha_L}(t) = \langle \Psi_{\mathbf{k}\alpha_L}(t) | x | \Psi_{\mathbf{k}\alpha_L}(t) \rangle = \sum_{bb' (b \neq b')} [P_{\mathbf{k}\alpha_L}(t)]_{bb'} X_{b'b} \quad (8)$$



for state  $\alpha_L$ , where  $x$  is the  $x$ -component of position vector of electron. Here,  $P_{\mathbf{k}\alpha_L}(t)$  represents the associated microscopic interband polarization corresponding to an off-diagonal element of a reduced density matrix, and  $[P_{\mathbf{k}\alpha_L}(t)]_{sp} = [P_{\mathbf{k}\alpha_L}(t)]_{ps}$  because of  $X_{sp} = X_{ps}$ .<sup>49</sup> The interband polarization in the  $\omega$ -domain is introduced as:  $\tilde{P}_{\mathbf{k}\alpha_L}^{(N)}(\omega) = (0|D_{\mathbf{k}\alpha_L}(t)|N)/X_{sp}$  with  $\tilde{P}_{\mathbf{k}\alpha_L}^{(-N)}(\omega) = [\tilde{P}_{\mathbf{k}\alpha_L}^{(N)}(\omega)]^*$ . Below, we examine  $\tilde{\mathcal{D}}(\mathbf{k}) \equiv \text{Re}[\tilde{P}_{\mathbf{k}\alpha_L}^{(1)}(\omega)]$  as a function of  $\mathbf{k}$  in the 2D-BZ; neither  $\tilde{P}_{\mathbf{k}\alpha_L}^{(N \neq \pm 1)}(\omega)$  nor  $\text{Im}[\tilde{P}_{\mathbf{k}\alpha_L}^{(\pm 1)}(\omega)]$  show significant variance in the BZ with the change in  $F_x$ . It is stated that  $\tilde{\mathcal{D}}(\mathbf{k})$  precisely reflects the degree of parity hybridization in the 2D-BZ that results from the I-symmetry breaking due to the laser irradiation.

The calculated results of  $\tilde{\mathcal{D}}(\mathbf{k})$  are shown in Figs. 4d-4f, Figs. 5d-5f, and Figs. 6d-6f along with  $\mathcal{E}(k_x)$  in the vicinity of  $F_x^\Gamma$ ,  $F_x^{X_2}$ , and  $F_x^{X_1}$ , respectively, where a black solid line shows a contour indicating the boundary of  $\tilde{\mathcal{D}}(\mathbf{k}) = 0$ , which is hereafter termed as the zero contour. It is readily seen that the zero-contour projected onto the  $k_x$ -axis coincides with the segment of the 1D-BZ at which an edge state manifests itself irrespective of being topological or not. To be more specific, the edge state is discerned where a vertical line that is parallel to the  $k_y$ -axis at a certain  $k_x$  crosses the zero contour twice. For instance, as seen in Fig. 6f, the vertical line crosses this contour twice except around the  $\bar{\Gamma}$ -point, and the edge state emerges in the corresponding range of  $k_x$ .

Another contour indicating  $\tilde{\mathcal{D}}(\mathbf{k}) = 0$  is discerned around the  $M$ -points in Figs. 4d-4f, which is shown by a black dashed line; this causes no edge state and is attributed to the anticrossing between the bands of  $s(-1)$  and  $p(2)$ . There is a critical difference between  $\tilde{\mathcal{D}}(\mathbf{k}^{j(c)})$  with  $j(c) = \Gamma, X_2, X_1$  and  $\tilde{\mathcal{D}}(\mathbf{k}^M)$  as functions of  $F_x$ , as is shown in Fig. 7. A singular nature of  $\tilde{\mathcal{D}}(\mathbf{k}^{j(c)})$  is evidently confirmed by seeing that there is discontinuity of  $\tilde{\mathcal{D}}(\mathbf{k}^{j(c)})$  at  $F_x = F_x^{j(c)}$ , namely,  $\tilde{\mathcal{D}}(\mathbf{k}^{j(c)})|_{F_x \rightarrow F_x^{j(c)} + 0} \neq \tilde{\mathcal{D}}(\mathbf{k}^{j(c)})|_{F_x \rightarrow F_x^{j(c)} - 0}$ , whereas  $\tilde{\mathcal{D}}(\mathbf{k}^M)$  is always a continuous function of  $F_x$  even in the vicinity of the anticrossing around the  $M$ -point. Such a singularity is attributed to an adiabatic interchange of the constituent of wavefunction  $\Psi_{\mathbf{k}\alpha_L}(t)$  between  $p(1)$  and  $s(-1)$  at  $\mathbf{k}^{j(c)}$ . This brings  $\Psi_{\mathbf{k}\alpha_L}(t)$  to be discontinuous, leading to an abrupt change of parity with the traverse of  $F_x$  at  $F_x^{j(c)}$ . In other words, a diabatic point is formed at  $\mathbf{k}^{j(c)}$  as a monopole of Berry curvature,<sup>50</sup> when a massless Floquet Dirac fermion is created at the closure of gap.

**Bulk-edge correspondence and  $\mathbb{Z}_2$  topological number.** Next, we show that the shape of the zero contour in the BZ also enables us to determine whether the state  $\alpha_L$  is

topological or not. It is appropriate to redefine the zero contour as that appears except around the M-points. This divides the BZ into two regions,  $R_I$  and  $R_O$ , where  $R_{I/O}$  is defined as the region with/without the  $\Gamma$ -point inside it. Here, let  $\nu_{I/O}$  be the number of high-symmetry points belonging to  $R_{I/O}$  and the first quadrant of the BZ coincidentally, where  $\nu_I + \nu_O = 4$ . To be specific, as shown in Figs. 4d-4f, a pinhole (shown by a black filled circle) emerges at the  $\Gamma$ -point at  $F_x^\Gamma$  as the boundary of the phase transition between the non-topological state with  $\nu_I = 0$  (in  $F_x > F_x^\Gamma$ ) and the topological state with  $\nu_I = 1$  (in  $F_x^{X_2} < F_x < F_x^\Gamma$ ). Similarly, as shown in Figs. 5d-5f, the band crossing emerging at the  $X_2$ -point at  $F_x^{X_2}$  changes  $\nu_I$  by one, leading to the further topological transition to the new phase with  $\nu_I = 2$  (in  $F_x^{X_1} < F_x < F_x^{X_2}$ ). The further change of  $\nu_I$  to 3 (in  $F_x < F_x^{X_1}$ ) is caused by the phase transition at the  $X_1$ -point, as shown in Figs. 6d-6f. Accordingly, it is inferred that a topological index  $\nu$  of the  $\mathbb{Z}_2 = (-)^\nu$  number is given by  $\nu = \nu_I \pmod{2} = \nu_O \pmod{2}$ . Therefore, the topology relevant to the shape of the zero contour provides the bulk-edge correspondence in the system of concern and determines the topological nature of the Floquet state.

## Discussion

This work shows that the nearly resonant laser-excitation gives rise to the fourfold accidental degeneracies at the high-symmetry points, and the resulting Floquet DSM states host unconventional Dirac-Tamm states that are transformable into either topological edge states or Tamm states with the change of  $F_x$ . A stress is put on the key role of this excitation mechanism maximizing the degree of hybridization of different parity states, though there are few studies thus far that have mentioned its significance for revealing unexplored topological nature.<sup>26</sup> It should be further stressed that the interband polarization reflecting such parity hybridization provides the close correspondence between the topological number of Floquet bulk band  $\alpha_L$  and the location of the concomitant edge states in the 1D-BK. Therefore, it is expected that the interband polarization fulfills a role of the guiding principle of Floquet engineering<sup>30,51</sup> for topological materials by means of optical controls using cw lasers.

Moreover, the studies on the interrelation between a Tamm state and a topological edge state have been rapidly noticed, because the state-of-the-art techniques of fabrication of optical waveguide arrays and photonic crystals have made it possible to create both edge states by mimicking the one-dimensional Su-Schrieffer-Hegger model<sup>39–42,45,52,53</sup> and more compli-

cated systems.<sup>43,44,46</sup> In this work, both of the edge states are transformed in a continuous manner as a function of the single parameter  $F_x$  without changing the composition and structure of the system, which draws a sharp distinction from these existing studies. It is also expected that the present findings make an important contribution of understanding the interrelation between both edge states from a unified perspective.

Finally, we make a couple of comments on this study. First, as  $F_x$  increases, it is more likely that the Floquet bands are somewhat modified by effects of the bandgap renormalization and the Rabi energy renormalization due to the many-body Coulomb interaction.<sup>49</sup> Second, by using a heavier element leading to a stronger spin-orbit interaction, the anti-crossing between  $p(1)$  and  $s(-1)$  is made greater and the edge state formed within this gap is made more pronounced. Third, it would be hard to experimentally realize the findings obtained here, as it stands, because of the 2D topological materials in non-equilibrium. Time- and- angle-resolved photoemission spectroscopy and cyclotron resonance are considered as promising methods under the existing circumstances. The former can resolve photo-induced band gaps in 3D Floquet topological materials,<sup>27,54</sup> while the latter makes it possible to observe a precise band structure of a 2D DSM in the HgTe quantum well with critical thickness.<sup>55</sup>

## Methods

Numerical calculations for a wavefunction  $\Psi_{\mathbf{k}\alpha}(t)$  of Floquet state  $\alpha$  and the associated quasienergy  $E_\alpha(\mathbf{k})$  are implemented by relying on the Fourier-Floquet expansion of Eq. (4), followed by diagonalizing the Floquet matrix  $\tilde{L}_{nn'}(\mathbf{k}, \omega)$ . The explicit expressions of matrix elements of it are given in Supplementary Note 1. The maximum number of photons ( $N_p$ ) incorporated in this calculation is three, namely,  $n, n' = -N_p \sim N_p$ , and the numerical convergence is checked by using a greater value of  $N_p$ . The following material parameters in the units of a.u. are employed for actual calculations:<sup>56</sup>  $\epsilon_s = -\epsilon_p = 0.01$ ,  $t_{ss} = t_{pp} = 0.001$ ,  $t_{sp} = 0.002$ ,  $a = 12.21$ , and  $X_{sp} = 34.63$ .  $\omega$  and  $E_g$  are set to be 0.0114 and 0.012, respectively.

---

\* hino@ims.tsukuba.ac.jp

- <sup>1</sup> Kane, C. L. & Mele, E. J. Quantum Spin Hall Effect in Graphene. *Phys. Rev. Lett.* **95** 226801-226804 (2005).
- <sup>2</sup> Bernevig, B. A., Hughes T. L. & Zhang, S. C. Quantum Spin Hall Effect and Topological Phase Transition in HgTe Quantum Wells. *Science* **314** 1757-1761 (2006).
- <sup>3</sup> Hasan, M. Z. & Kane, C. L. Topological insulators. *Rev. Mod. Phys.* **82** 3045-3067 (2010).
- <sup>4</sup> Qi, X. L. & Zhang, C. H. Topological insulators and superconductors. *Rev. Mod. Phys.* **85** 1057-1110 (2011).
- <sup>5</sup> Ozawa, T. *et al.* Topological photonics. *Rev. Mod. Phys.* **91** 015006 (87 pages) (2019).
- <sup>6</sup> Castro Neto, A. H. *et al.* The electronic properties of graphene. *Rev. Mod. Phys.* **81** 109-162 (2009).
- <sup>7</sup> Wehling; T. O., Black-Schaffer, A. M. & Balatsky, A. V. Dirac materials. *Advances in Physics* **63** 1-76 (2014).
- <sup>8</sup> Armitage, N. P. & Mele E. J. Weyl and Dirac semimetals in three-dimensional solids. *Rev. Mod. Phys.* **90** 015001 (63 pages) (2018).
- <sup>9</sup> Murakami, S. *et al.* Tuning phase transition between quantum spin Hall and ordinary insulating phases. *Phys. Rev. B* **76** 205304 (6 pages) (2007).
- <sup>10</sup> Murakami, S. Phase transition between the quantum spin Hall and insulator phases in 3D: emergence of a topological gapless phase. *New J. Phys.* **9** 356 (15 pages) (2007); Corrigendum. *New J. Phys.* **10** 029802 (2 pages) (2008).
- <sup>11</sup> Young, S. M. *et al.* Dirac Semimetal in Three Dimensions. *Phys. Rev. Lett.* **108** 140405 (5 pages) (2012).
- <sup>12</sup> Young, S. M. & Kane, C. L. Dirac Semimetals in Two Dimensions. *Phys. Rev. Lett.* **115** 126803(5 pages) (2015).
- <sup>13</sup> Wang, Z. *et al.* Dirac semimetal and topological phase transitions in  $A_3Bi$  ( $A = Na, K, Rb$ ). *Phys. Rev. B* **85** 195320 (5 pages) (2012).
- <sup>14</sup> Wang, Z. *et al.* Three-dimensional Dirac semimetal and quantum transport in  $Cd_3As_2$ . *Phys. Rev. B* **88** 125427 (6 pages) (2013).
- <sup>15</sup> Yang, B. -J. & Nagaosa, N. Classification of stable three-dimensional Dirac semimetals with nontrivial topology. *Nat. Comm.* **5** 4898 (10 pages) (2014).
- <sup>16</sup> Park, S. & Yang, B. -J. Classification of accidental band crossings and emergent semimetals in two-dimensional noncentrosymmetric systems. *Phys. Rev. B* **96** 125127 (13 pages) (2017).

- <sup>17</sup> Yi, H. *et al.* Evidence of Topological Surface State in Three-Dimensional Dirac Semimetal  $\text{Cd}_3\text{As}_2$ . *Sci. Rep.* **4** 6106 (6 pages) (2014).
- <sup>18</sup> Xu, S. -Y. *et al.* Discovery of a Weyl fermion semimetal and topological Fermi arcs. *Science* **349** 613-617 (2015).
- <sup>19</sup> Kargariana, M., Randeria, M. & Lu, Y. -M. Are the surface Fermi arcs in Dirac semimetals topologically protected?. *PNAS* **113** 8648-8652 (2016).
- <sup>20</sup> Doh, H. & Choi, H. J. Dirac-semimetal phase diagram of two-dimensional black phosphorus. *2D Mater.* **4** 025071 (8 pages) (2017).
- <sup>21</sup> Ramankutty, S. V. *et al.* Electronic structure of the candidate 2D Dirac semimetal  $\text{SrMnSb}_2$ : a combined experimental and theoretical study. *SciPost Phys.* **4** 010 (25 pages) (2018).
- <sup>22</sup> Luo, W. *et al.* Two-dimensional Topological Semimetals Protected by Symmorphic Symmetries. *Phys. Rev. B* **101** 195111 (25 pages) (2020).
- <sup>23</sup> Shirley, J. H. Solution of the Schrödinger Equation with a Hamiltonian Periodic in Time. *Phys. Rev.* **138** B979-B987 (1965).
- <sup>24</sup> Kitagawa, T., Berg, E., Rudner, M. & Demler, E. Topological characterization of periodically driven quantum systems. *Phys. Rev. B* **82** 235114 (12 pages) (2010).
- <sup>25</sup> Zhenghao, G. *et al.* Floquet Spectrum and Transport through an Irradiated Graphene Ribbon. *Phys. Rev. Lett.* **107**, 216601-216605 (2011).
- <sup>26</sup> Lindner, N. H., Refael, G. & Galitski, V. Floquet topological insulator in semiconductor quantum wells. *Nat. Phys.* **7** 490-495 (2011).
- <sup>27</sup> Wang, Y. H., Steinberg, H., Jarillo-Herrero, P. & Gedik, N. Observation of Floquet-Bloch States on the Surface of a Topological Insulator. *Science* **342** 453-457 (2013).
- <sup>28</sup> Rechtsman, M. C. *et al.* Photonic Floquet topological insulators. *Nature* **496** 196-200 (2013).
- <sup>29</sup> Höbener, H. *et al.* Creating stable FloquetWeyl semimetals by laser-driving of 3D Dirac materials. *Nat. Comm.* **8** 13940 (8 pages) (2016).
- <sup>30</sup> Hansen, M. *et al.* Topological edge-state engineering with high-frequency electromagnetic radiation. *Phys. Rev. B* **96** 205127 (9 pages) (2017).
- <sup>31</sup> Nakagawa, M., Slager, R. -J., Higashikawa, S. & Oka, T. Wannier representation of Floquet topological states. *Phys. Rev. B* **101** 075108 (16 pages) (2020).
- <sup>32</sup> Autler, S. H. & Townes, C. H. Stark Effect in Rapidly Varying Fields. *Phys. Rev.* **100** 703-722 (1955).

- <sup>33</sup> Knight, P. L. & Milonni, P. W. The Rabi frequency in optical spectra. *Phys. Rep.* **66**, 21-107 (1980).
- <sup>34</sup> Sie, E. J. *et al.* Valley-selective optical Stark effect in monolayer WS<sub>2</sub>. *Nat. Mat.* **14** 290-294 (2015).
- <sup>35</sup> Tamm, I. On the possible bound states of electrons on a crystal surface. *Phys. Z. Sov. Union* **1** 733-746 (1932).
- <sup>36</sup> Shockley, W. On the Surface States Associated with a Periodic Potential. *Phys. Rev.* **56** 317-323 (1939).
- <sup>37</sup> Ohno, H. *et al.* Observation of "Tamm States" in Superlattices. *Phys. Rev. Lett.* **64**, 2555-2558 (1990).
- <sup>38</sup> Volkov, V. A. & Enaldiev, V. V. Surface States of a System of Dirac Fermions: A Minimal Model. *J. Exp. Theor. Phys* **122** 608-620 (2016).
- <sup>39</sup> Longhi, S. Zak phase of photons in optical waveguide lattices. *Opt. Lett.* **38** 3716-3719 (2013).
- <sup>40</sup> Wang, L. *et al.* Zak phase and topological plasmonic Tamm states in one-dimensional plasmonic crystals. *Opt. Express* **26** 28963-28975 (2018).
- <sup>41</sup> Chen, T. *et al.* Distinguishing the Topological Zero Mode and Tamm Mode in a Microwave Waveguide Array. *Ann. Phys. (Berlin)* **531** 1900347 (5 pages)(2019).
- <sup>42</sup> Yang, Y. & Pan, Y. Engineering Zero Modes, Fano Resonance, and Tamm Surface States in the Waveguide-Array Realization of the Modified Su-Schrieffer-Heeger Model. *Opt. Express* **27** 32900-32911 (2019).
- <sup>43</sup> Tsurimaki, Y. *et al.* Topological Engineering of Interfacial Optical Tamm States for Highly Sensitive Near-Singular-Phase Optical Detection. *ACS Photonics* **5** 929938 (2018).
- <sup>44</sup> Lu, H. *et al.* Topological insulator based Tamm plasmon polaritons. *APL Photonics* **4** 040801 (7 pages) (2019).
- <sup>45</sup> Henriques, J. C. G. *et al.* Topological Photonic Tamm-States and the Su-Schrieffer-Heeger Model. *Phys. Rev. A* **101** 043811 (13 pages) (2020).
- <sup>46</sup> Latyshev, Y. I. *et al.* Transport of Massless Dirac Fermions in Non-topological Type Edge States. *Sci. Rep.* **4** 7578 (6 pages) (2014).
- <sup>47</sup> Pantaléon, P. A., Carrillo-Bastos, R & Xian, Y. Topological Magnon Insulator with a Kekulé Bond Modulation. *J. Phys: Cond. Mat.* **31** 085802 (8 pages) (2019).
- <sup>48</sup> Yan, B. Topological states on the gold surface. *Nat. Commun.* **6** 10167(6 pages) (2015).

- <sup>49</sup> Haug, H. & Koch, S. W. *Quantum Theory of the Optical and Electronic Properties of Semiconductors*. Chaps. 12 and 15 (World Scientific, fifth edition, 2009).
- <sup>50</sup> Berry M.V. Aspects of Degeneracy. In: Casati G. (eds) *Chaotic Behavior in Quantum Systems. NATO ASI Series (Series B: Physics)* **120** 123-140 (Springer, Boston, MA, 1985).
- <sup>51</sup> Kennes, D. M. *et al.* Floquet Engineering in Quantum Chains. *Phys. Rev. Lett.* **120** 127601 (5 pages) (2018).
- <sup>52</sup> Su, W. P., Schrieffer, J. R. & Heeger, A. Soliton excitations in polyacetylene. *Phys. Rev. B* **22** 2099-2111 (1980).
- <sup>53</sup> Heeger, A. J., Kivelson, S. Schrieffer, J. R. & Su, W. P. Solitons in conducting polymers. *Rev. Mod. Phys.* **60** 781-850 (1988).
- <sup>54</sup> Sobota, J. A. *et al.* Ultrafast Optical Excitation of a Persistent Surface-State Population in the Topological Insulator Bi<sub>2</sub>Se<sub>3</sub>. *Phys. Rev. Lett.* **108** 117403 (5 pages) (2012).
- <sup>55</sup> Shuvaev, A. M. *et al.* Band Structure of Two-dimensional Dirac Semimetal from Cyclotron Resonance. *Phys. Rev. B* **96** 155434 (7 pages) (2017).
- <sup>56</sup> Novik, E. G. *et al.* Band structure of semimagnetic Hg<sub>1-y</sub>Mn<sub>y</sub>Te quantum wells. *Phys. Rev. B* **72** 035321 (12 pages) (2005).

## Acknowledgments

This work was supported by JSPS KAKENHI Grant No. JP19K03695. The authors are grateful to Prof. J. Fujioka for fruitful discussion.

## Competing financial interests

The authors declare no competing financial interests.

## Author contributions

K.H. conceived the main ideas and supervised the project. B.Z. carried out the main parts of the numerical calculations, and N.M. carried out the rest parts of them. All authors discussed and interpreted the results. K.H. wrote the paper and B.Z. prepared the figures with contribution from all authors.

## Additional information

Supplementary information is available for the paper at <https://xxx>. Correspondence and requests for materials should be addressed to K.H.

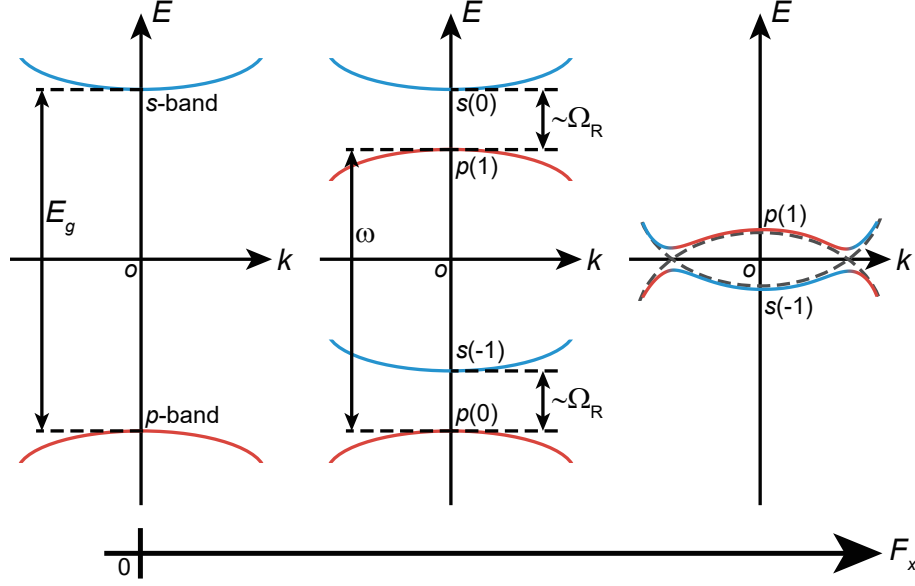


FIG. 1. **Scheme of the nearly resonant optical-excitation followed by the OSE.** (Left) The original energy allocation of the  $p$ -band (red solid line) and the  $s$ -band (blue solid line) with energy gap  $E_g$ . (Center) With the application of cw-laser with frequency  $\omega$  and constant electric field  $F_x$ , the OSE causes quasienergy-splitting of the order of the Rabi frequency  $\Omega_R$  between a pair of photodressed bands,  $s(n-1)$  and  $p(n)$ , with  $n = 0, 1$ . (Right) With the further increase in  $F_x$ , a pair of bands of  $p(1)$  and  $s(-1)$  undergoes inversion with anticrossing. Band crossing takes place at a certain  $F_x$ , as shown by a dashed line.



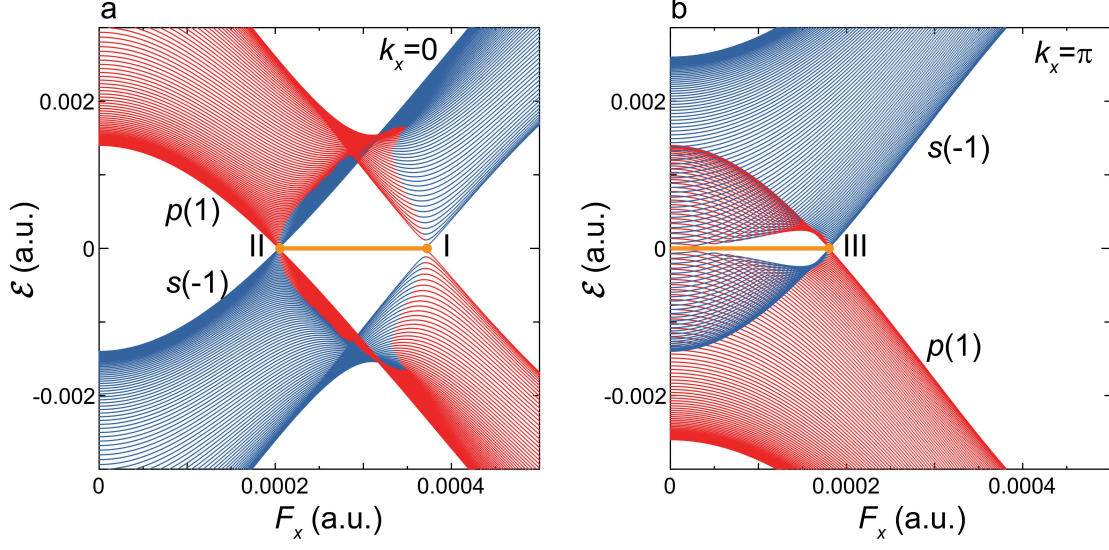


FIG. 2. **Band inversion and band crossing.** (a) Shown are  $\mathcal{E}_{p(1)}(k_x)$  and  $\mathcal{E}_{s(-1)}(k_x)$  for  $k_x = 0$  as a function of  $F_x$ . The two quasienergy bands  $p(1)$  and  $s(-1)$  (shown by red and blue lines, respectively) cross when  $F_x$  is fine-tuned at the positions of I and II. Shown are the zero modes (Dirac nodes) by a yellow solid line. (b) The same as the panel (a) but for  $k_x = \pi$ . The two quasienergy bands cross when  $F_x$  is fine-tuned at the position of III.

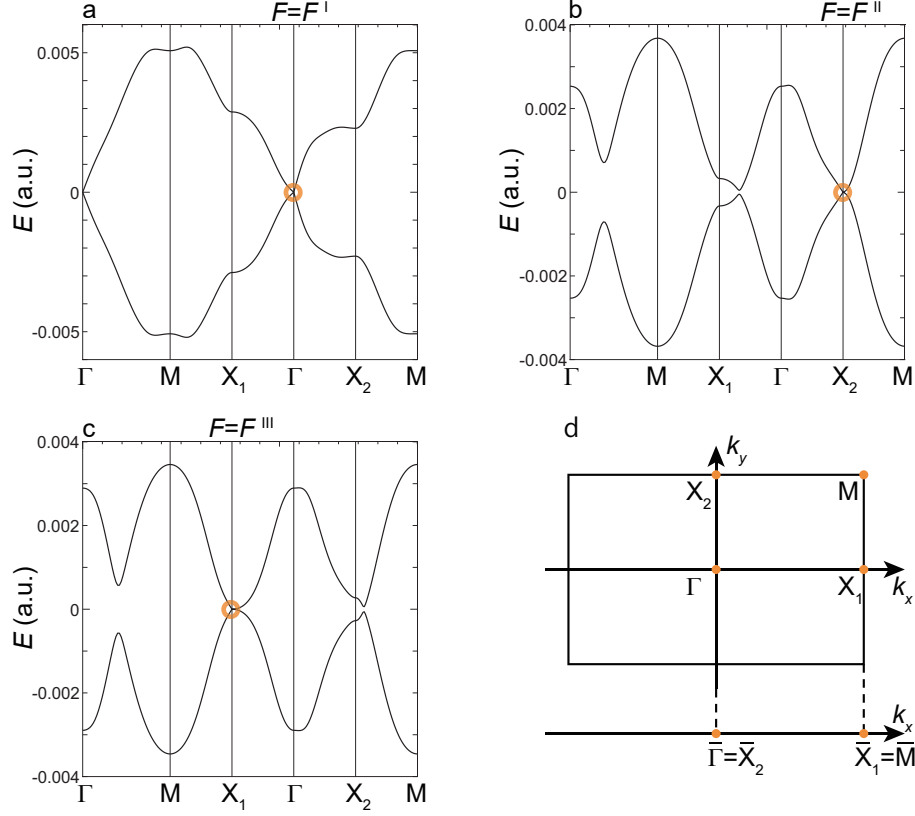


FIG. 3. **Quasienergy dispersion of 2D-bulk band  $E(\mathbf{k})$ .** (a) Shown is  $E(\mathbf{k})$  at  $F_x^I$ , where  $E_{p(1)}(\mathbf{k})$  and  $E_{s(-1)}(\mathbf{k})$  are degenerate at the  $\Gamma$  point. (b) The same as the panel (a) but at  $F_x^{II}$  with the degeneracy at the  $X_2$  point. (c) The same as the panel (a) but at  $F_x^{III}$  with the degeneracy at the  $X_1$  point. (d) Shown are the high-symmetry points of  $\Gamma, X_2, X_1$  and  $M$  in the 2D-BZ with their projection onto the  $k_x$ -axis denoted as  $\bar{\Gamma}, \bar{X}_2, \bar{X}_1$  and  $\bar{M}$ , respectively.

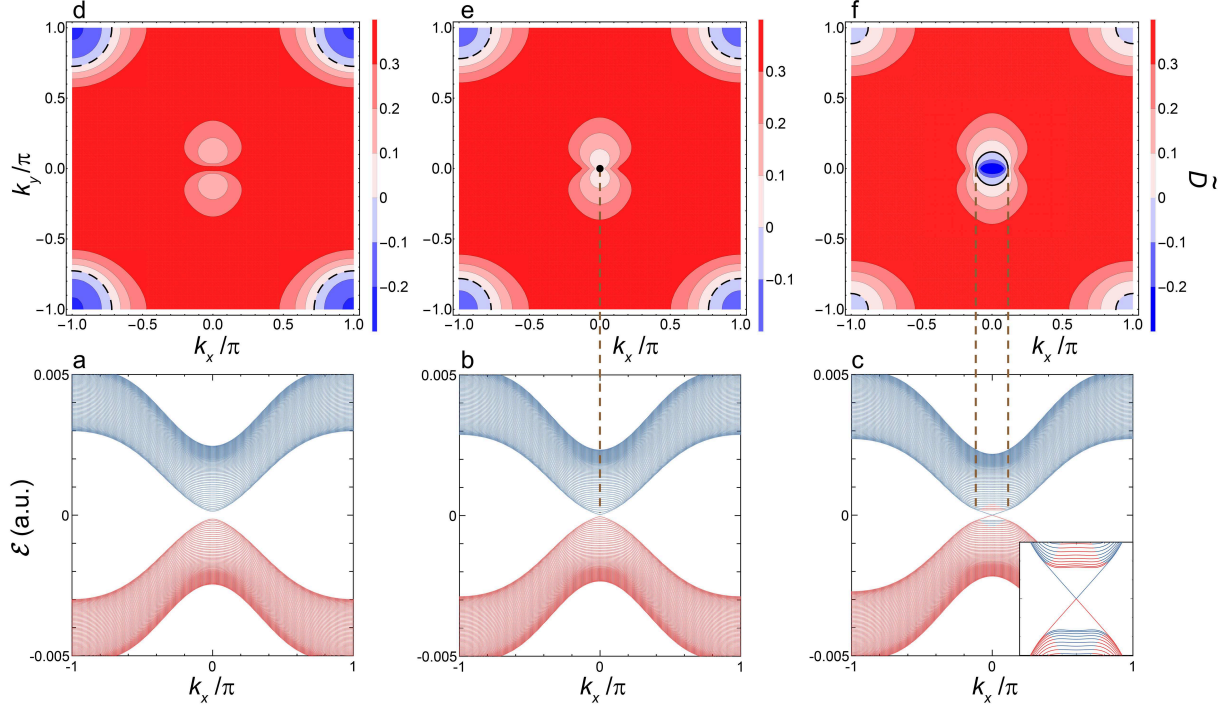


FIG. 4. **Quasienergy dispersion of  $\mathcal{E}(k_x)$  and interband polarization  $\tilde{\mathcal{D}}(\mathbf{k})$  in the vicinity of  $F_x^\Gamma$ .** (a) Shown are  $\mathcal{E}_{p(1)}(k_x)$  and  $\mathcal{E}_{s(-1)}(k_x)$  as functions of  $k_x$  at  $F_x > F_x^\Gamma$ . The two quasienergy bands  $p(1)$  and  $s(-1)$  are shown by red and blue lines, respectively. (b) The same as the panel (a) but at  $F_x^\Gamma$ . (c) The same as the panel (a) but at  $F_x < F_x^\Gamma$ . Inset: the expanded view of these two bands in the vicinity of the  $\bar{\Gamma}$ -point. (d) Shown is a contour map  $\tilde{\mathcal{D}}(\mathbf{k})$  in the  $(k_x, k_y)$ -plane at  $F_x > F_x^\Gamma$ . Contours indicating the boundary of  $\tilde{\mathcal{D}}(\mathbf{k}) = 0$  are shown by black dashed lines. (e) The same as the panel (d) but at  $F_x^\Gamma$ . Besides, a pinhole indicating  $\tilde{\mathcal{D}}(\mathbf{k}) = 0$  at the  $\Gamma$ -point is shown by a black filled circle. The vertical dashed line shows the projection of  $\tilde{\mathcal{D}}(\mathbf{k}) = 0$  (the pinhole) onto the  $k_x$ -axis shown in the panel (b). (f) The same as the panel (d) but at  $F_x < F_x^\Gamma$ . Contours indicating the boundary of  $\tilde{\mathcal{D}}(\mathbf{k}) = 0$  are shown by black solid and dashed lines. The vertical dashed lines show the projection of  $\tilde{\mathcal{D}}(\mathbf{k}) = 0$  (the zero contour) onto the  $k_x$ -axis shown in the panel (c).

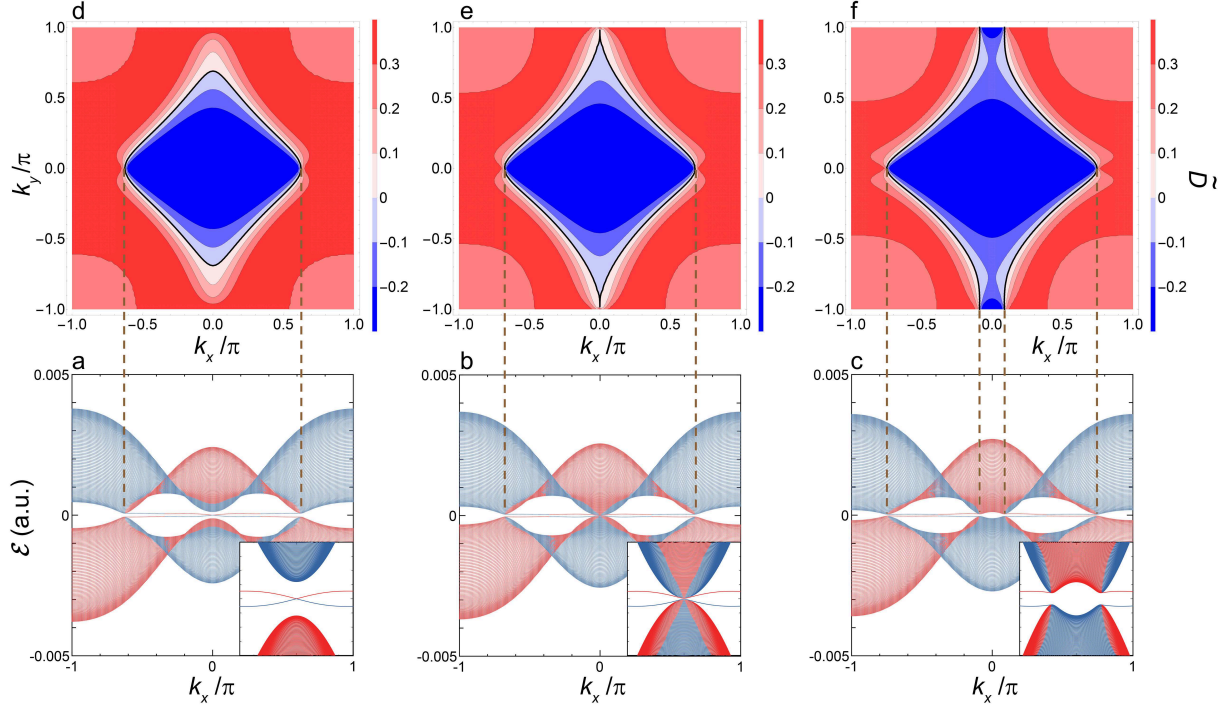


FIG. 5. **Quasienergy dispersion of  $\mathcal{E}(k_x)$  and interband polarization  $\tilde{\mathcal{D}}(\mathbf{k})$  in the vicinity of  $F_x^{X_2}$ .** (a) Shown are  $\mathcal{E}_{p(1)}(k_x)$  and  $\mathcal{E}_{s(-1)}(k_x)$  as functions of  $k_x$  at  $F_x > F_x^{X_2}$ . The two quasienergy bands  $p(1)$  and  $s(-1)$  are shown by red and blue lines, respectively. Inset: the expanded view of these two bands in the vicinity of the  $\bar{X}_2$ -point. (b) The same as the panel (a) but at  $F_x^{X_2}$ . (c) The same as the panel (a) but at  $F_x < F_x^{X_2}$ . (d) Shown is a contour map  $\tilde{\mathcal{D}}(\mathbf{k})$  in the  $(k_x, k_y)$ -plane at  $F_x > F_x^{X_2}$ . The vertical dashed lines show the projection of  $\tilde{\mathcal{D}}(\mathbf{k}) = 0$  (the zero contour) onto the  $k_x$ -axis shown in the panel (a). (e) The same as the panel (d) but at  $F_x^{X_2}$  and with the zero contour projected onto the  $k_x$ -axis shown in the panel (b). (f) The same as the panel (d) but at  $F_x < F_x^{X_2}$  and with the zero contour projected onto the  $k_x$ -axis shown in the panel (c).

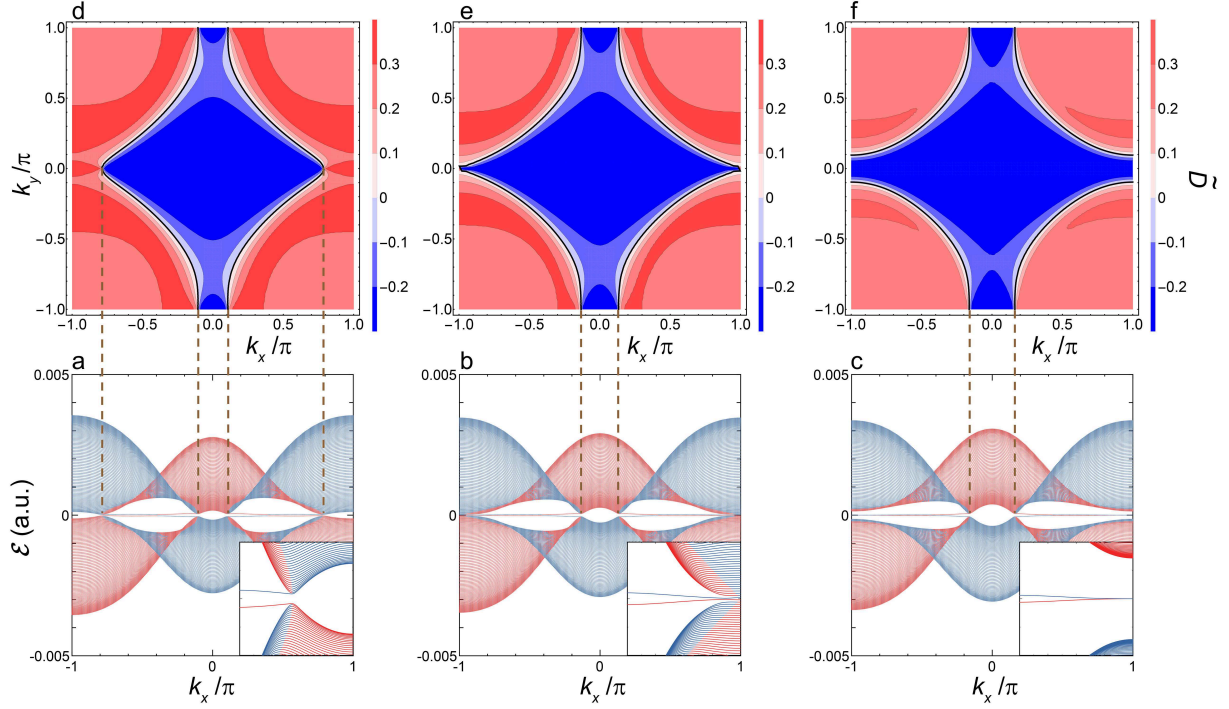


FIG. 6. **Quasienergy dispersion of  $\mathcal{E}(k_x)$  and interband polarization  $\tilde{\mathcal{D}}(\mathbf{k})$  in the vicinity of  $F_x^{X_1}$ .** (a) Shown are  $\mathcal{E}_{p(1)}(k_x)$  and  $\mathcal{E}_{s(-1)}(k_x)$  as functions of  $k_x$  at  $F_x > F_x^{X_1}$ . The two quasienergy bands  $p(1)$  and  $s(-1)$  are shown by red and blue lines, respectively. Inset: the expanded view of these two bands in the vicinity of the  $\bar{X}_1$ -point. (b) The same as the panel (a) but at  $F_x^{X_1}$ . (c) The same as the panel (a) but at  $F_x < F_x^{X_1}$ . (d) Shown is a contour map  $\tilde{\mathcal{D}}(\mathbf{k})$  in the  $(k_x, k_y)$ -plane at  $F_x > F_x^{X_1}$ . The vertical dashed lines show the projection of  $\tilde{\mathcal{D}}(\mathbf{k}) = 0$  (the zero contour) onto the  $k_x$ -axis shown in the panel (a). (e) The same as the panel (d) but at  $F_x^{X_1}$  and with the zero contour projected onto the  $k_x$ -axis shown in the panel (b). (f) The same as the panel (d) but at  $F_x < F_x^{X_1}$  and with the zero contour projected onto the  $k_x$ -axis shown in the panel (c).

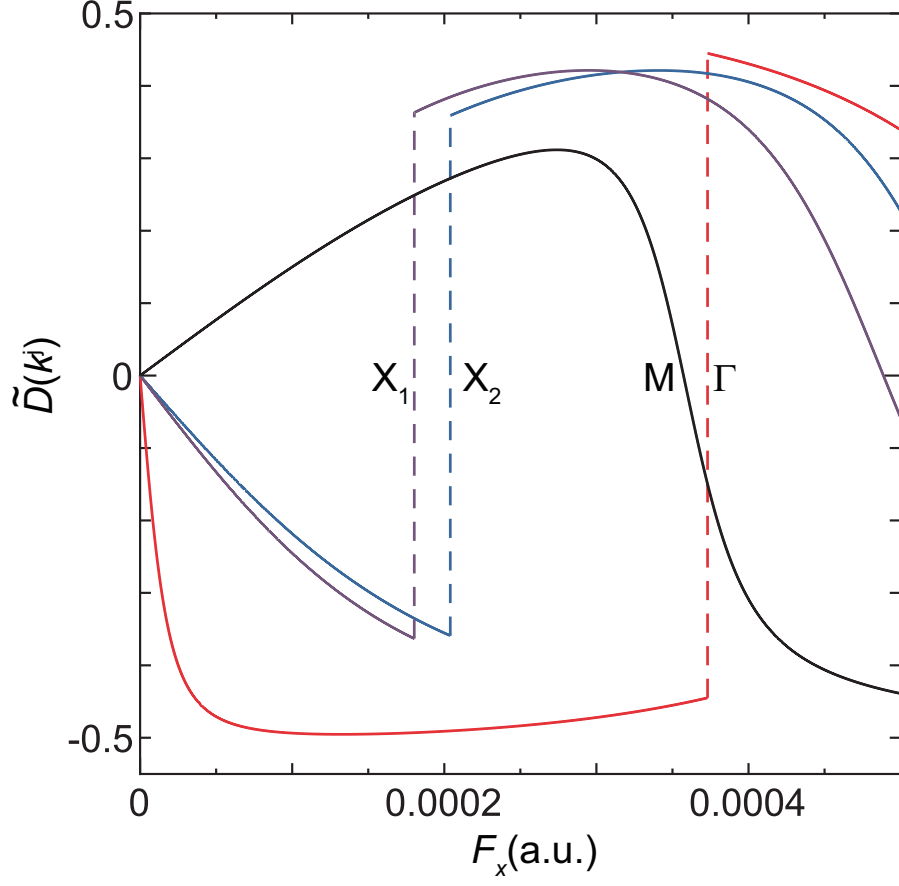


FIG. 7. Variance of interband polarization  $\tilde{D}(k^j)$  at high-symmetry points as function of  $F_x$ . Interband polarizations at  $\Gamma$ ,  $X_2$ ,  $X_1$ , and  $M$ -points are depicted by red, blue, purple, and black lines, respectively.